Journal of
Computational and Theoretical Nanoscience
Vol. 6, 1808–1826, 2009

Modeling of Plasmonic Waveguide Components and Networks

Georgios Veronis[1,*], Şükrü Ekin Kocabaş[2], David A. B. Miller[2], and Shanhui Fan[2]

[1] *Department of Electrical and Computer Engineering and Center for Computation and Technology, Louisiana State University, Baton Rouge, LA 70803, USA*
[2] *Ginzton Laboratory, Stanford University, Stanford, CA 94305, USA*

We review some of the recent advances in the simulation of plasmonic devices, drawing examples from our own work in metal-insulator-metal (MIM) plasmonic waveguide components and networks. We introduce the mode-matching technique for modeling of MIM waveguide devices. We derive the complete set of orthogonal modes that the MIM waveguide supports and use it to apply the mode-matching technique to the analysis of plasmonic waveguide networks. We also introduce several different equivalent models for plasmonic waveguide components, such as the characteristic impedance model for deep subwavelength MIM waveguides, the scattering matrix description of MIM waveguide junctions, and equivalent circuit models. The model abstraction provided by these equivalent models is important for the analysis and synthesis of device functions, as illustrated with the design of a waveguide mode converter.

Keywords: Plasmonics, Surface Plasmons, Mode-Matching, Equivalent Circuits, Scattering Matrix, Characteristic Impedance.

CONTENTS

1. INTRODUCTION

Surface plasmons are electromagnetic waves that propagate along the interface of a metal and a dielectric. In surface plasmons light interacts with the free electrons of the metal which oscillate collectively in response to the applied field.[1] Recently, nanometer scale metallic devices have shown the potential to manipulate light at subwavelength scales using surface plasmons. This could lead to photonic circuits of nanoscale dimensions. The use of nano-metallic structures could also bridge the size mismatch between modern electronic components with critical dimensions on the order of tens of nanometers and the micrometer scaled optical devices.[2]

Plasmonic waveguides have shown the potential to guide subwavelength optical modes at metal–dielectric interfaces. Several different plasmonic waveguiding structures have been proposed,[3–8] such as metallic nanowires[4,5] and metallic nanoparticle arrays.[6,7] Most of these structures support a highly-confined mode only near the surface plasmon frequency. In this regime, the optical mode typically has low group velocity and short propagation length. It has been shown however that a metal-insulator-metal (MIM) structure with a dielectric region thickness of ~100 nm supports a propagating mode with a nanoscale modal size at a wavelength range extending from DC to visible.[9] Thus, such a waveguide could be potentially important in providing an interface between conventional optics and subwavelength electronic and optoelectronic devices. There have been several theoretical studies of MIM waveguides in the literature.[9–18] Because of the

*Author to whom correspondence should be addressed.

 1546-1955/2009/6/1808/019 doi:10.1166/jctn.2009.1244

Georgios Veronis received the B.S. degree in electrical engineering from the National Technical University of Athens, Greece, in 1997, and the M.S. and Ph.D. degrees in electrical engineering from Stanford University, Stanford, CA, in 1999 and 2002 respectively. He was an engineering research associate at the Ginzton Laboratory at Stanford University. He is currently an assistant professor jointly at the Department of Electrical & Computer Engineering and the Center for Computation & Technology at Louisiana State University, Baton Rouge, LA. He has published more than 25 refereed journal papers, and is the holder of 1 U.S. patent. His research interests include the theoretical analysis of nanophotonic and plasmonic devices, and computational electromagnetics. Dr. Veronis is a member of IEEE and OSA.

Şükrü Ekin Kocabaş received the B.S. and M.S. degrees in electrical engineering from Bilkent University, Ankara, Turkey and Stanford University, Stanford, CA, USA in 2002 and 2004 respectively. Currently, he is a Ph.D. student majoring in electrical engineering with a minor in physics. He has been a member of IEEE since 2000. His main research interest is modeling and fabrication of nanophotonic optoelectronic devices.

David A. B. Miller received the B.Sc. degree from St Andrews University, and the Ph.D. degree from Heriot-Watt University, in 1979, both in Physics. He was with Bell Laboratories, from 1981 to 1996, as a department head from 1987, latterly of the Advanced Photonics Research Department. He is currently the W. M. Keck Professor of Electrical Engineering at Stanford University, Stanford, CA, the Director of the Solid State and Photonics Laboratory at Stanford and a Co-Director of the Stanford Photonics Research Center. He also served as Director of the Ginzton Laboratory at Stanford from 1997–2006. His research interests include nanophotonic and quantum-confined optoelectronic physics and devices, and fundamentals and applications of optics in information sensing, switching, and processing. He has published more than 200 scientific papers, delivered more than 100 conference invited talks, and holds 62 patents. Dr. Miller has served as a Board member for both the Optical Society of America (OSA) and the IEEE Lasers and Electro-Optics Society (LEOS), and in various other society and conference committees. He was President of the IEEE Lasers and Electro-Optics Society in 1995. He has also served on Boards for various photonics companies. He was awarded the Adolph Lomb Medal and the R. W. Wood Prize from the OSA, the International Prize in Optics from the International Commission for Optics, and the IEEE Third Millennium Medal. He is a Fellow of the Royal Societies of London and Edinburgh, OSA, APS, and IEEE, and holds honorary degrees from the Vrije Universiteit Brussel and Heriot-Watt University.

Shanhui Fan is an associate professor of electrical engineering at Stanford University. He received his Ph.D. in 1997 in theoretical condensed matter physics from the Massachusetts Institute of Technology (MIT), and was a research scientist at the Research Laboratory of Electronics at MIT prior to his appointment at Stanford. His research interests are in computational and theoretical studies of solid state and photonic structures and devices, especially photonic crystals, microcavities, and nanophotonic circuits and elements. He has published over 140 refereed journal articles, has given over 100 invited talks, and was granted 28 US patents. Professor Fan received a National Science Foundation Career Award (2002), a David and Lucile Packard Fellowship in Science and Engineering (2003), the National Academy of Sciences Award for Initiative in Research (2007), and the Adolph Lomb medal from the Optical Society of America (2007). Dr. Fan is fellow of OSA and APS, a senior member of IEEE, and a member of SPIE.

predicted attractive properties of MIM waveguides, people have also started to explore such structures experimentally. In particular, Dionne et al.[19] have recently demonstrated waveguiding in a quasi-two-dimensional MIM geometry experimentally, showing clear evidence of a subwavelength guided mode with substantial propagation distances.

Most of the theoretical studies of nanoscale plasmonic devices involve the use of general purpose electromagnetic simulation techniques. These techniques are able to simulate devices of arbitrary geometry and material composition. On the other hand, as described in the next section, these techniques typically require numerical grids with resolution of tens to thousands of grid points per wavelength, depending on the application. They are therefore not suitable for the design and optimization of multi-component optical circuits. One approach to address this problem is the development of special-purpose simulation techniques with superior computational efficiency for a specific class of problems. Previously, for example, in the modeling of photonic crystal devices, it has been shown that the use of Wannier functions results in several orders of magnitude speedup in the optimization of photonic crystal circuits.[20] A second approach is the development of equivalent models with only a few dynamic variables, which are nevertheless capable of describing complex optical processes in photonic devices in detail. For example, in the modeling of photonic crystal devices, it has been shown that such models can be derived with the use of coupled mode theory,[21, 22] and perturbation theory.[22, 23]

In this context, here, we provide a review of some of our own recent research activities aiming to advance the theory and simulation of plasmonic waveguide devices through the development of efficient special-purpose simulation techniques and equivalent models. We first give an overview of the challenges involved in modeling of plasmonic devices, and we briefly examine two general purpose simulation techniques which are widely used for modeling of plasmonic waveguide devices. We then introduce the mode-matching technique for modeling of MIM waveguide devices. We derive the complete set of orthogonal modes that the MIM waveguide supports and use it to apply the mode-matching technique to the analysis of plasmonic waveguide networks. We show that this special purpose simulation technique is far more efficient for this class of problems than general purpose electromagnetic simulation techniques. Finally, we introduce several different equivalent models for plasmonic waveguide components, such as the characteristic impedance model for deep subwavelength MIM waveguides, the scattering matrix description of MIM waveguide junctions, and equivalent circuit models. We show that the model abstraction provided by these equivalent models is important for the analysis and synthesis of device functions, and we illustrate this with the design of a mode converter.

2. CHALLENGES INVOLVED IN MODELING OF PLASMONIC DEVICES

Surface plasmons can be described by macroscopic electromagnetic theory, i.e., Maxwell's equations, if the electron mean free path in the metal is much shorter than the plasmon wavelength. This condition is usually fulfilled at optical frequencies.[24] Assuming an $\exp(i\omega t)$ harmonic time dependence of all field quantities, Maxwell's curl equations in the frequency domain take the form

$$\nabla \times \mathbf{E}(\mathbf{r}) = -i\omega\mu_0 \mathbf{H}(\mathbf{r}) \tag{1}$$

$$\nabla \times \mathbf{H}(\mathbf{r}) = i\omega\epsilon_0 \epsilon_r(\mathbf{r})\mathbf{E}(\mathbf{r}) \tag{2}$$

In macroscopic electromagnetic theory, bulk material properties, such as the relative dielectric constant $\epsilon_r(\mathbf{r})$, are used to describe objects irrespective of their size. However, for particles of nanoscale dimensions a more fundamental description of their optical and electronic properties may be required.[25]

Analytical methods, such as Mie theory,[26] can only be applied to planar geometries or to objects with very high symmetry (spheres, infinite cylinders) and have therefore limited importance in the analysis of plasmonic devices and structures. Thus, the analysis of plasmonic devices is mostly based on numerical simulation techniques.

Numerical modeling of plasmonic devices involves several challenges specific to plasmonics which need to be addressed. The dielectric constant of metals at optical wavelengths is complex, i.e., $\epsilon_r(\omega) = \epsilon_{\mathrm{Re}}(\omega) + i\epsilon_{\mathrm{Im}}(\omega)$ and is a complicated function of frequency.[27] Thus, several simulation techniques which are limited to lossless, non-dispersive materials are not applicable to plasmonic devices. In addition, in time-domain methods the dispersion properties of metals have to be approximated by suitable analytical expressions.[28] In most cases the *Drude model* is invoked to characterize the frequency dependence of the metallic dielectric function[29]

$$\epsilon_{r,\,\mathrm{Drude}}(\omega) = 1 - \frac{\omega_p^2}{\omega(\omega + i\gamma)} \tag{3}$$

where ω_p, γ are frequency-independent parameters. However, the Drude model approximation is valid over a limited wavelength range.[29] The range of validity of the Drude model can be extended by adding Lorentzian terms to Eq. (3) to obtain the *Lorentz–Drude model*[29]

$$\epsilon_{r,\,\mathrm{LD}}(\omega) = \epsilon_{r,\,\mathrm{Drude}} + \sum_{j=1}^{k} \frac{f_j \omega_j^2}{(\omega_j^2 - \omega^2) - i\omega\gamma_j} \tag{4}$$

where ω_j and γ_j stand for the oscillator resonant frequencies and bandwidths respectively, and f_j are weighting factors. Physically, the Drude and Lorentzian terms are related to intraband (free-electron) and interband (bound-electron) transitions respectively.[29] Even though the Lorentz–Drude model extends the range of validity of

analytical approximations to metallic dielectric constants, it is not suitable for description of sharp absorption edges observed in some metals, unless a very large number of terms is used.[29] In particular, the Lorenz-Drude model cannot approximate well the onset of interband absorption in noble metals (Ag, Au, Cu) even if five Lorentzian terms are used.[29] In Figure 1 we compare the Drude and Lorentz–Drude models with experimental data for silver. We observe that even a five-term Lorentz–Drude model with optimal parameters results in a factor of two error at certain frequencies. An alternative approach is the use of an analytical expression based on multiple complex-conjugate pole-residue pairs.[30] It has been shown that, when such an approach is used with time-domain methods, it can lead to substantial savings in both memory and computation time.[30]

In addition, in surface plasmons propagating along the interface of a metal and a dielectric, the field is concentrated at the interface, and decays exponentially away from the interface in both the metal and dielectric regions.[1] Thus, for numerical methods based on discretization of the fields on a numerical grid, a very fine grid resolution is required at the metal-dielectric interface to adequately resolve the local fields. In addition, several plasmonic devices are based on components of subwavelength dimensions.[1] In fact, most of the potential applications of surface plasmons are related to subwavelength optics. The nanoscale feature sizes of plasmonic devices pose an extra challenge to numerical simulation techniques.

We illustrate the challenges involved in modeling plasmonic devices using a simple example. We consider an infinite periodic array of silver cylinders illuminated by a plane wave at normal incidence (inset of Fig. 2(a)). We use the finite-difference frequency-domain method, described in more detail below, to calculate the transmission of the periodic array. This method allows us to directly use experimental data for the frequency-dependent dielectric constant of metals, including both the real and imaginary parts, with no further approximation. The fields are discretized on a uniform two-dimensional grid with grid size $\Delta x = \Delta y = \Delta l$. In Figure 2(a) we show the calculated transmission as a function of frequency. We also show the transmission of the structure calculated with

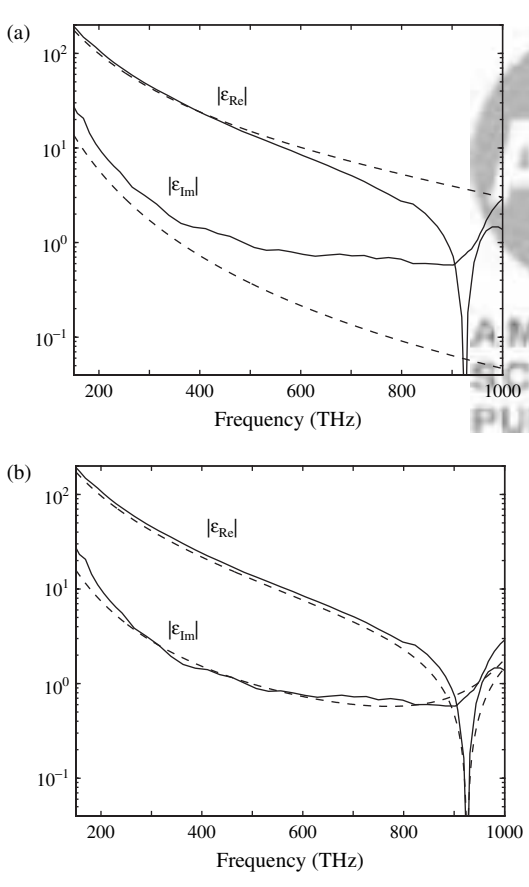

Fig. 1. Real and imaginary part of the dielectric constant of silver at optical frequencies. The solid lines show experimental data.[27] The dashed lines show values calculated using (a) the Drude model, (b) the Lorentz–Drude model with five Lorentzian terms. The parameters of the models are obtained through an optimization procedure.[29]

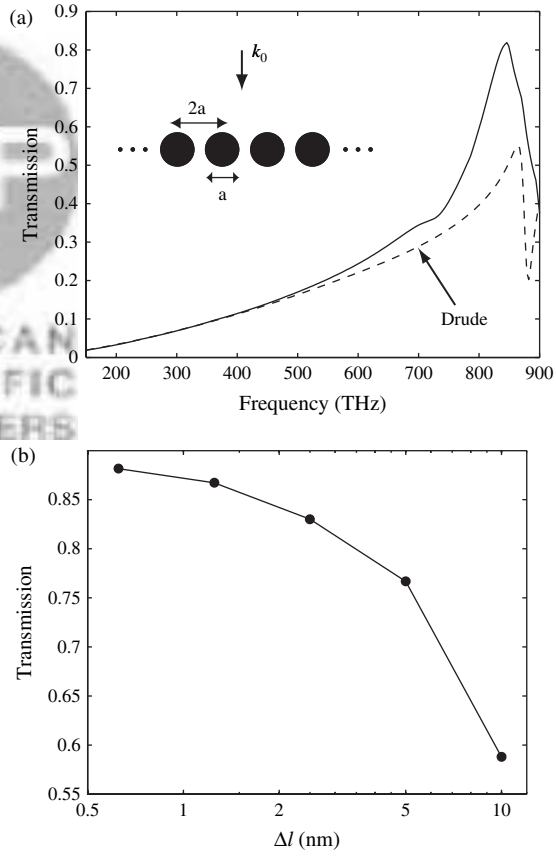

Fig. 2. (a) Calculated transmission spectrum of an infinite array of silver cylinders (shown in the inset) for normal incidence and TM polarization. Results are shown for $a = 100$ nm. The dashed line shows the transmission spectrum calculated using the Drude model with parameters $\omega_p = 1.37 \times 10^{16}\,\mathrm{sec}^{-1}$, $\gamma = 7.29 \times 10^{13}\,\mathrm{sec}^{-1}$. (b) Calculated transmission at 855 THz as a function of the spatial grid size Δl.

the Drude model of Eq. (3). We observe that the use of the Drude model results in substantial error. In general, the Drude model parameters are chosen to minimize the error in the dielectric function in a given frequency range.[31] However, this approach gives accurate results in a limited wavelength range, as illustrated in this example. In general, the complicated dispersion properties of metals at optical frequencies pose a challenge in modeling of plasmonic devices not encountered in modeling of low- or high-index-contrast dielectric devices.

In Figure 2(b) we show the calculated transmission at a specific wavelength of $\lambda_0 = 351$ nm as a function of the spatial grid size Δl. We observe that a grid size of $\Delta l \simeq 1$ nm is required in this case to yield reasonably accurate results. The required grid size is directly related to the decay length of the fields at the metal-dielectric interface. In general, modeling of plasmonic devices requires much finer grid resolution than modeling of low- or high-index-contrast dielectric devices, due to the high localization of the field at metal-dielectric interfaces of plasmonic devices. The required grid size depends on the shape and feature size of the modeled plasmonic device, the metallic material used and the operating frequency.

3. GENERAL PURPOSE SIMULATION METHODS FOR PLASMONIC WAVEGUIDE DEVICES

Here we briefly examine two general purpose electromagnetic simulation techniques which are widely used for modeling of plasmonic waveguide devices, the finite-difference frequency-domain (FDFD) and the finite-difference time-domain (FDTD) methods. We also examine how they address the challenges mentioned above. Other general purpose simulation techniques for modeling of plasmonic waveguide devices include the Green dyadic method,[4] the finite-element method,[32] and the method of lines.[33]

3.1. Finite-Difference Frequency-Domain Method

In finite-difference methods, derivatives in differential equations are approximated by finite differences. To approximate the derivative $df/dx|_{x_0}$ we consider Taylor series expansions of $f(x)$ about the point x_0 at the points $x_0 + \Delta x$ and $x_0 - \Delta x$ and obtain[28]

$$\left.\frac{df}{dx}\right|_{x_0} = \frac{f(x_0+\Delta x) - f(x_0-\Delta x)}{2\Delta x} + O[(\Delta x)^2] \quad (5)$$

Equation (5) shows that a *central-difference* approximation of the first derivative is *second-order accurate*, meaning that the remainder term in Eq. (5) approaches zero as the square of Δx.

In finite-difference methods a continuous problem is approximated by a discrete one. Field quantities are defined on a discrete grid of nodes. The rectangular grid with node coordinates $\mathbf{r}_{ijk} = (x_i, y_j, z_k)$ is the simplest and most commonly-used. A field quantity at nodal location $\mathbf{r}_{ijk}$ is denoted for convenience as $f_{ijk} = f(\mathbf{r}_{ijk})$. Based on Eq. (5), the first derivative can be approximated by the following central-difference formula

$$\left.\frac{df}{dx}\right|_i \simeq \frac{f_{i+1} - f_{i-1}}{2\Delta x} \quad (6)$$

which is second-order accurate, based on the discussion above, if the rectangular grid is uniform, i.e., $x_i = i\Delta x$. Similarly, the second derivative can be approximated by the formula

$$\left.\frac{d^2f}{dx^2}\right|_i \simeq \frac{f_{i+1} - 2f_i + f_{i-1}}{(\Delta x)^2} \quad (7)$$

which is also second-order accurate on a uniform grid.[28]

By replacing derivatives in differential equations with their finite-difference approximations, we obtain algebraic equations which relate the value of the field at a specific node to the values at neighboring nodes. To solve Maxwell's equations with the FDFD method, we discretize the system of the three coupled scalar partial differential equations obtained from the wave equation for the electric field

$$\nabla \times \nabla \times \mathbf{E}(\mathbf{r}) - \epsilon_r(\mathbf{r})\frac{\omega^2}{c^2}\mathbf{E}(\mathbf{r}) = -i\omega\mu_0\mathbf{J}(\mathbf{r}) \quad (8)$$

For simplicity we consider here two-dimensional problems with TE polarization. For TE polarization we have $\mathbf{E} = E_z\hat{z}$ and the wave equation for the electric field becomes[32, 34]

$$\left[\frac{\partial^2}{\partial x^2} + \frac{\partial^2}{\partial y^2} + k_0^2\epsilon_r(x, y)\right]E_z(x, y) = -i\omega\mu_0 J_z(x, y) \quad (9)$$

For simplicity we consider a uniform rectangular grid with $x_i = i\Delta x$, $y_j = j\Delta y$, and replace the derivatives in Eq. (9) with their finite-difference approximations of Eq. (7) to obtain

$$\frac{f_{i+1,j} - 2f_{i,j} + f_{i-1,j}}{(\Delta x)^2} + \frac{f_{i,j+1} - 2f_{i,j} + f_{i,j-1}}{(\Delta y)^2} + k_0^2\epsilon_{ri,j}f_{i,j} = A_{i,j} \quad (10)$$

where $f = E_z$ and $A = -i\omega\mu_0 J_z$. Thus, application of finite-difference approximations at the node location $\mathbf{r}_{ij} = (x_i, y_j)$ results in a linear algebraic equation which relates the field $f_{i,j}$ to the fields at the four adjacent nodes $f_{i+1,j}$, $f_{i-1,j}$, $f_{i,j+1}$, $f_{i,j-1}$. By applying the finite-difference approximation to all nodes of the grid we obtain a system of linear equations of the form $\mathbf{Ax} = \mathbf{b}$, where $\mathbf{b}$ is determined by the source current $\mathbf{J}$. Since the equation for the field at each point involves only the fields at the four (six in three dimensions, two in one dimension) adjacent points, the resulting system matrix is extremely sparse.[34]

FDFD can be used to model plasmonic devices with arbitrary geometries. In addition, FDFD is a frequency-domain technique and can thus treat arbitrary material

dispersion. Nonuniform and/or nonorthogonal grids are required in FDFD for efficient treatment of curved surfaces and rapid field decays at metal-dielectric interfaces. In FDFD, as in all other methods which are based on discretization of the differential form of Maxwell's equations in a finite volume, absorbing boundary conditions (ABCs) are required so that waves are not artificially reflected at the boundaries of the computational domain.[28, 32] Very efficient and accurate ABCs such as the perfectly matched layer (PML) have been demonstrated.[35] As mentioned above, FDFD results in extremely sparse systems of linear equations. Such problems can be solved efficiently if direct or iterative sparse matrix techniques are used.[32, 34]

3.2. Finite-Difference Time-Domain Method

The FDTD method[28] solves directly Maxwell's time-dependent curl equations

$$\nabla \times \mathbf{E} = -\mu_0 \frac{\partial \mathbf{H}}{\partial t} \tag{11}$$

$$\nabla \times \mathbf{H} = \epsilon_0 \epsilon_r \frac{\partial \mathbf{E}}{\partial t} \tag{12}$$

so that both space and time have to be discretized. The standard FDTD is based on the Yee algorithm.[28] As mentioned in the previous section, central-difference approximations are second-order accurate. To achieve second-order accuracy in time, the Yee algorithm uses a leapfrog arrangement.[28] **E** fields are calculated at $t = n\Delta t$ using previously calculated and stored **H** fields. Then **H** fields are calculated at $t = (n + 1/2)\Delta t$ using the previously calculated and stored **E** fields, and the process continues until time-stepping is concluded. Applying this scheme to Eq. (11) we obtain

$$\mathbf{H}|^{n+1/2} = \mathbf{H}|^{n-1/2} - \frac{\Delta t}{\mu_0} \nabla \times \mathbf{E}|^{n} \tag{13}$$

We observe that the leapfrog scheme yields central-difference in time and therefore second-order accurate approximations. In addition, since **E**(**H**) fields are obtained from previously calculated and stored **H**(**E**) fields, the time-stepping is fully explicit, meaning that we do not have to solve a system of simultaneous equations.[28]

To achieve second-order accuracy in space, FDTD uses a special grid, known as the *Yee lattice*, where every **E** component is surrounded by four **H** components and every **H** component is surrounded by four **E** components.[28] Based on this arrangement, discretization of the x-component of Eq. (11) gives

$$H_x|^{n+1/2}_{i,j,k} = H_x|^{n-1/2}_{i,j,k} + \frac{\Delta t}{\mu_0}\left[\frac{E_y|^{n}_{i,j,k+1/2} - E_y|^{n}_{i,j,k-1/2}}{\Delta z} - \frac{E_z|^{n}_{i,j+1/2,k} - E_z|^{n}_{i,j-1/2,k}}{\Delta y}\right] \tag{14}$$

We observe that, using the Yee lattice, all spatial finite-difference expressions are central and therefore second-order accurate. Similar finite-difference equations are obtained by discretizing the other components of Eqs. (11) and (12). In summary, FDTD is an explicit numerical scheme which is second-order accurate both in time and in space (in uniform media).

3.2.1. Treatment of Dispersive Media in FDTD

One of the major challenges in FDTD modeling of metals at optical frequencies is the treatment of the metallic dispersion properties. As mentioned above, in time-domain methods the dielectric constants of dispersive media have to be approximated by suitable analytical expressions. The most common algorithm for modeling dispersive materials with FDTD is the *auxiliary differential equation* (ADE) method.[28, 36] In dispersive materials $\epsilon(\omega)$ relates **E** and **D**

$$\mathbf{D} = \epsilon(\omega)\mathbf{E} \tag{15}$$

ADE is based on integrating an ordinary differential equation in time that relates $\mathbf{D}(t)$ to $\mathbf{E}(t)$, concurrently with Maxwell's equations. This equation is derived by taking the inverse Fourier transform of Eq. (15).

We consider here a simple example where the dielectric constant $\epsilon_r(\omega)$ consists of a single Lorentzian term, i.e.,

$$\epsilon_r(\omega) = \frac{\omega_0^2}{(\omega_0^2 - \omega^2) - i\omega\gamma_0} \tag{16}$$

If we substitute Eq. (16) into Eq. (15) and take the inverse Fourier transform, we obtain a second-order differential equation relating **D** and **E**

$$\omega_0^2 \mathbf{D} + \gamma_0 \frac{\partial \mathbf{D}}{\partial t} + \frac{\partial^2 \mathbf{D}}{\partial t^2} = \omega_0^2 \epsilon_0 \mathbf{E} \tag{17}$$

Equation (17) is discretized using a second-order accurate central-difference scheme similar to those described above. We note that, if the ADE method is used, **E** is obtained from **H** in two steps. First, **D** is obtained from **H** by solving the finite-difference approximation of

$$\nabla \times \mathbf{H} = \frac{\partial \mathbf{D}}{\partial t} \tag{18}$$

Second, **E** is obtained from **D** by solving the finite-difference approximation of Eq. (17). Calculation of the finite-difference expressions of the first and second time derivatives of **D** in Eq. (17) requires the storage of 2 previous values of **D**. In other words not only $\mathbf{D}|^{n+1}$ but also $\mathbf{D}|^{n}$ and $\mathbf{D}|^{n-1}$ are required to obtain **E** from **D**.

Another approach to model dispersive materials with FDTD is the *recursive convolution* (RC) method.[28, 36]

FDTD is a finite-difference method, so its performance in modeling plasmonic devices is similar to the performance of FDFD. However, there are some major differences. First, as already mentioned above, in time-domain

methods the dispersion properties of metals have to be approximated by suitable analytical expressions which introduce substantial error in broadband calculations. In addition, the implementation of the ADE or RC methods requires additional computational cost and extra memory storage.[28, 36] On the other hand, in FDTD it is possible to obtain the entire frequency response with a single simulation by exciting a broadband pulse and calculating the Fourier transform of both the excitation and the response.[28]

4. MODE-MATCHING METHOD

In this section, we introduce the mode-matching technique for MIM waveguide devices. The mode-matching technique[37] is commonly used in the microwave and optical domains.[38–41] We derive the complete set of orthogonal modes that the MIM waveguide supports and use it to apply the mode-matching technique to the calculation of scattering at the junction between two guides with different cross sections.

4.1. Spectrum of MIM Waveguides

The mode-matching method is based on expanding the fields in terms of the modes of the waveguides. In this context here we derive the modal structure (spectrum) of the MIM waveguide.[42] We will specifically focus on the even modes of the waveguide, for which the *transverse magnetic* (TM) field component is an even function of the transverse coordinate, x. The reason why we focus on even modes is that we will be analyzing the scattering of the fundamental, even mode of the MIM waveguide—which is also a TM mode[10, 11, 15]—off of a symmetric junction with a different sized MIM waveguide. Due to the symmetry of the problem at hand, even modes will be sufficient. Evenness of the function is achieved by putting a fictitious *perfect electric conductor* (PEC) at the $x = 0$ plane of the waveguide, which forces the tangential electric field E_z to be an odd function, and the magnetic field H_y to be an even function of x. In other words, the modes of this fictitious waveguide with the PEC at $x = 0$ are mathematically the same as the even modes of the actual waveguide of interest, and so we will work with this hypothetical waveguide. The geometry is as shown in Figure 3(a). ϵ_m refers to the permittivity of the metal region and ϵ_i of the insulator region. At infrared frequencies, ϵ_m (Fig. 1) is a complex number with a large, negative real part and a relatively small imaginary part (the sign of which is determined by the time convention used, being negative for an $\exp(i\omega t)$ time dependence).

We begin with Maxwell's equations (Eqs. (1), (2)). The MIM waveguide is a two dimensional structure which does not have any variation in the y direction. Therefore, we can eliminate all the derivatives with respect to y in Maxwell's equations. Furthermore, our study will be based on the TM

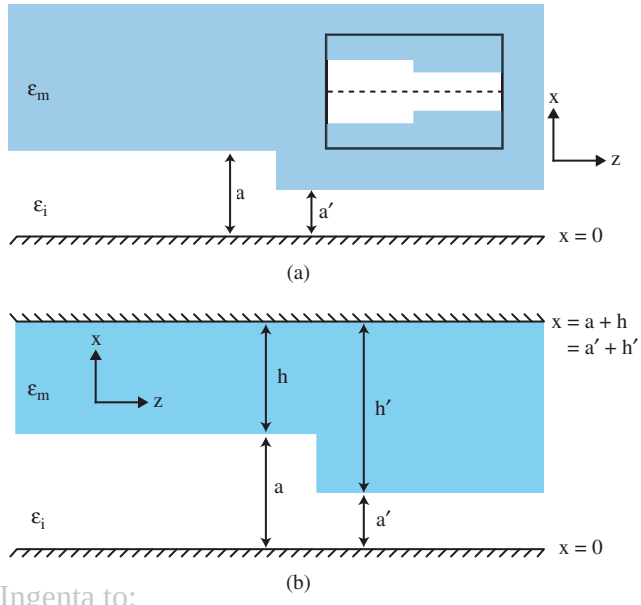

Fig. 3. (a) Geometry for the even modes of the MIM waveguide. The $x = 0$ plane contains a fictitious perfect electric conductor (PEC) to simplify the problem when dealing only with even TM modes of the guide. This fictitious MIM waveguide is equivalent to an actual guide with an insulator thickness of $2a$. The inset shows the equivalent symmetric junction of two MIM waveguides. Dashed line in the inset is the plane of symmetry, which is where the fictitious PEC layer is introduced. (b) Geometry for mode matching. $x = a+h$ plane of Figure 3(a) is terminated by a PEC which leads to a discretization of the continuous spectrum.

modes which only have the H_y, E_x and E_z field components. Also, the uniformity of the waveguide in the z direction leads to $\exp(-ik_z z)$ as the space dependence in z by using the separation of variables technique for differential equations (k_z may, however, be a complex number). After simplifying the curl equations in (1), (2), we have the following relationships between the different field components

$$\begin{aligned} i\omega\mu(x)H_y(x) &= ik_z E_x(x) + \frac{d}{dx}E_z(x) \\ ik_z H_y(x) &= i\omega\epsilon(x)E_x(x) \\ \frac{d}{dx}H_y(x) &= i\omega\epsilon(x)E_z(x) \end{aligned} \tag{19}$$

Using these equations we get the following differential equation for H_y

$$\left(\epsilon(x)\frac{d}{dx}\frac{1}{\epsilon(x)}\frac{d}{dx} + \omega^2\mu(x)\epsilon(x)\right)H_y = k_z^2 H_y \tag{20}$$

and since $E_z(0) = 0$ by the PEC wall at $x = 0$, the boundary condition for H_y under (19) becomes $dH_y(x)/dx|_{x=0} = 0$.

4.1.1. Point Spectrum

The dispersion equation that should be solved in order to find the k_z values for the modes of the MIM waveguide is

derived by satisfying the continuity of tangential electric and magnetic fields at material boundaries and applying the boundary conditions. We refer the reader to Refs. [43 and 9, 11, 44–46] for the details. The eigenvectors (ψ_n) and the dispersion equation for the corresponding eigenvalues ($k_{z,n}^2$) of (20) for the even TM modes of the MIM waveguide are

$$\psi_n(x) = H_0 \begin{cases} \dfrac{\cosh(\kappa_{i,n}x)}{\cosh(\kappa_{i,n}a)} & 0 < x < a \\ e^{-\kappa_{m,n}(x-a)} & a < x < \infty \end{cases} \quad (21)$$

$$\tanh(\kappa_{i,n}a) = -\frac{\kappa_{m,n}/\epsilon_m}{\kappa_{i,n}/\epsilon_i} \quad (22)$$

$$k_{z,n}^2 = \kappa_{m,n}^2 + \omega^2\mu\epsilon_m = \kappa_{i,n}^2 + \omega^2\mu\epsilon_i \quad (23)$$

where $\mathrm{Re}(\kappa_{m,n}) > 0$ so that $\psi_n(x)$ does not diverge and is integrable. Here n is a discrete index for the eigenvalues and the eigenfunctions.

4.1.2. Continuous Spectrum

In this section, we show that a continuous spectrum exists in the MIM waveguide. The utility of the continuous spectrum will be evident in the mode matching analysis.

The condition of square integrability of the modes can be replaced by the weaker condition of finiteness of the modes in their domain of definition.[47] For the MIM waveguide, this would imply a non-zero, yet finite electromagnetic field at infinity. These infinite-extent and, therefore, infinite energy, continuum modes (which can be normalized through the use of the Dirac delta distributions[48, 49]) are integrated to realize any physically possible finite energy field configuration. In this respect, such an approach is similar to the well-known Fourier transform methods, where finite energy functions are expanded in terms of the infinite energy exponentials.

Constraining fields to be finite, instead of zero, at infinity leads to the following field profile

$$\phi_\nu(x) = H_0 \begin{cases} \dfrac{\cosh(\kappa_{i,\nu}x)}{\cosh(\kappa_{i,\nu}a)} & 0 < x < a \\ \cosh(\kappa_{m,\nu}(x-a)) & \\ \quad + \zeta\sinh(\kappa_{m,\nu}(x-a)) & a < x < \infty \end{cases} \quad (24)$$

$$\zeta = \frac{\kappa_{i,\nu}/\epsilon_i}{\kappa_{m,\nu}/\epsilon_m}\tanh(\kappa_{i,\nu}a) \quad (25)$$

$$k_{z,\nu}^2 = \kappa_{m,\nu}^2 + \omega^2\mu\epsilon_m = \kappa_{i,\nu}^2 + \omega^2\mu\epsilon_i \quad (26)$$

which is calculated very similarly to the case of a dielectric slab.[43] Here ν is a continuous index for different functions in the continuous spectrum. For finite ϕ_ν, the arguments inside the hyperbolic functions for $x > a$ in (24), $\kappa_{m,\nu}$, should be purely imaginary which implies that $\mathrm{Re}(\kappa_{m,\nu}^2) < 0$ and $\mathrm{Im}(\kappa_{m,\nu}^2) = 0$. These conditions can be written in terms of $k_{z,\nu}$ by using (26) as

$$\mathrm{Re}(k_{z,\nu}^2 - \omega^2\mu\epsilon_m) < 0 \quad \text{and} \quad \mathrm{Im}(k_{z,\nu}^2 - \omega^2\mu\epsilon_m) = 0$$

Note that when (22) holds true, we have $\zeta = -1$ in (25) which makes (24) and (21) equivalent.

4.2. Mode Orthogonality

Orthogonality and completeness are two very valuable properties of modes, which make the mode matching technique possible. Here we use the *pseudo-inner product*, $[\cdot|\cdot]$, defined as[50]

$$[f|g] = \int_0^\infty f(x)g(x)dx$$

It can be shown that two different eigenfunctions, $\psi_1(x)$ and $\psi_2(x)$, corresponding to two different eigenvalues $k_{z,1}^2$ and $k_{z,2}^2$ are pseudo-orthogonal with $\epsilon^{-1}(x)$ weight[50, 51]

$$[\epsilon^{-1}\psi_1 \mid \psi_2] = 0 \quad (27)$$

From (19) it can be seen that $\epsilon^{-1}\psi_1$ is proportional to the transverse electric field component E_x of the mode. Therefore, the orthogonality condition can also be written as

$$\int_0^\infty E_{x1}(x)H_{y2}(x)dx = \int_{\mathbf{A}} \mathbf{E}_1(\mathbf{r}) \times \mathbf{H}_2(\mathbf{r}) \cdot d\mathbf{A} = 0$$

which is the well known modal orthogonality condition proved by the Lorentz reciprocity theorem,[52] where $\mathbf{A}$ denotes the cross section of the waveguide.

One can directly verify (27) by integration and using $\kappa_{m,1}^2 - \kappa_{m,2}^2 = \kappa_{i,1}^2 - \kappa_{i,2}^2$ which is a result of (23). The following orthogonality conditions between the elements of the point (ψ_n) and the continuous (ϕ_ν) spectrum can similarly be proved

$$[\epsilon^{-1}\psi_n|\phi_\nu] = 0 \quad \text{for all } n \text{ and } \nu$$

$$[\epsilon^{-1}\phi_\mu|\phi_\nu] = 0 \quad \text{for} \quad \nu \neq \mu$$

In the following sections, we will be working with fields at the junction of two different waveguides. For notational abbreviation we will use the following convention

$$e_{\{L,R\}}^{(i)} = E_{x,i}^{\{L,R\}}$$

$$h_{\{L,R\}}^{(i)} = H_{y,i}^{\{L,R\}}$$

where $\{L, R\}$ is used to denote the modes of the left and right side of the junction, which leads to the following orthogonality condition

$$[e_{\{L,R\}}^{(i)} \mid h_{\{L,R\}}^{(j)}] = \delta_{ij}\Omega_{\{L,R\}} \quad (28)$$

where δ_{ij} is the Kronecker delta function and Ω is the overlap integral of the electric and magnetic transverse fields.

Table I. Adjectives.

Signifier	Signified
Leaky	$\mathrm{Re}(\kappa_m) < 0$
Proper	$\mathrm{Re}(\kappa_m) > 0$
Improper	$\mathrm{Re}(\kappa_m) = 0$
Forward	$\mathrm{Re}(k_z) > 0$
Backward	$\mathrm{Re}(k_z) < 0$

After the classification and analysis of the MIM waveguide modes, we will now visualize different parts of its spectrum by finding the zeros of the respective dispersion equations through the use of the argument principle method.[53–58] We will use the adjectives in Table I to further differentiate between the modes.

Leaky modes are not normalizable and are not part of the spectrum. *Proper* modes can be normalized by the usual integration and they form the point spectrum. *Improper* modes can be normalized by using the Dirac delta functions, $\delta(x)$. They form the continuous spectrum. *Forward* modes have a positive phase velocity, whereas the *backward* modes have a negative phase velocity. We decide on the sign of $\mathrm{Re}(k_z)$ based on $\mathrm{Im}(k_z)$: By definition, all modes are propagating in the $+z$ direction. Therefore, in the limit $z \to \infty$, the fields should go to zero. Such a behavior is possible only if $\mathrm{Im}(k_z)$ is negative, since the fields have an $\exp(-ik_z z)$ dependence. The argument principle method gives us the κ_m value for the modes. By using (23) we get the k_z^2 value. We then calculate $(k_z^2)^{1/2}$ and choose the root which satisfies $\mathrm{Im}(k_z) < 0$.

In Figure 4 the spectrum of an idealized lossless silver-like MIM waveguide is shown on the plane of κ_m^2 for $\epsilon_m = -143.497$ which is the real part of the permittivity of silver at a wavelength λ of 1550 nm.[27,59] There are four real modes for $2a = \lambda/4$—TM_0, TM_2, TM_4, TM_6—indexed according to the number of zero crossings in H_y. There is also an infinite number of complex modes, which are those with eight and more zero crossings in the insulator region. These modes have a κ_m with a positive real part that is rather small compared to the imaginary part—this can also be deduced from the scale of the imaginary axis of Figure 4. The continuous spectrum is illustrated by the thick line which corresponds to $\mathrm{Re}(\kappa_m^2) < 0$ and $\mathrm{Im}(\kappa_m^2) = 0$. This line is also the branch cut of the square root function that is used to get κ_m from κ_m^2. The field profiles of the modes in the insulator region, as shown in the insets of Figure 4, look quite similar to the field profile of the even modes of a parallel plate waveguide with a plate separation of $2a$.

$\kappa_m^2 = 0$ is the bifurcation point for the point spectrum when ϵ_m is purely real. For positive κ_m^2, the point spectrum has real modes, whereas for negative κ_m^2, the

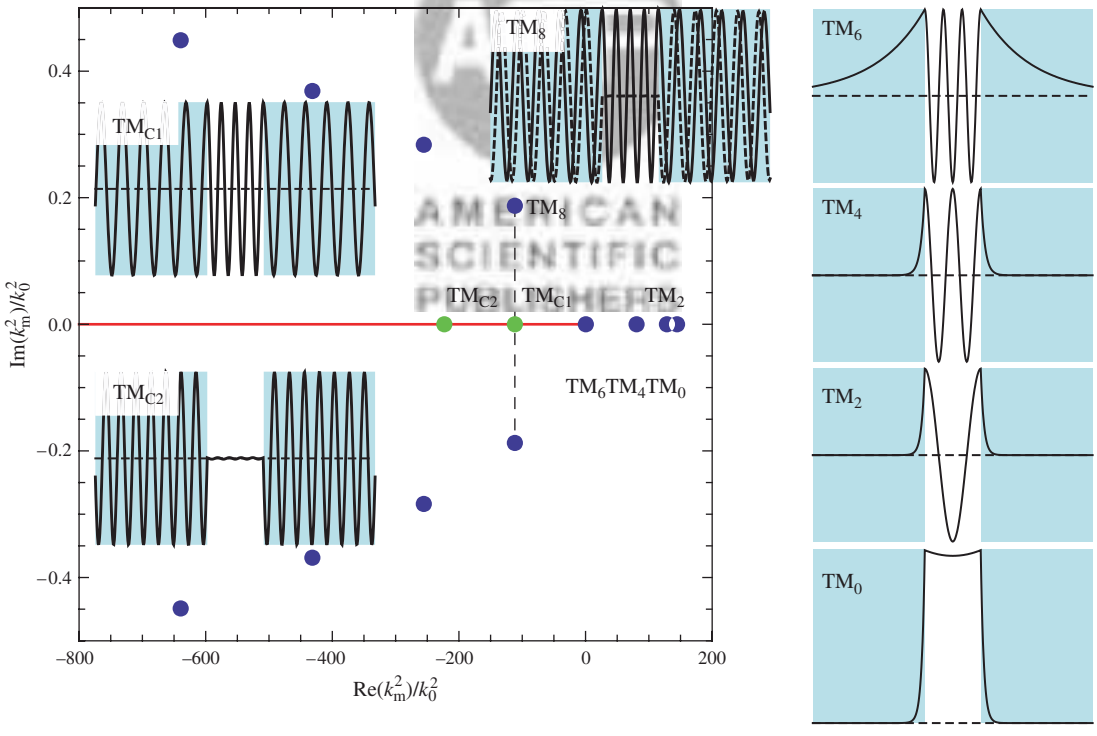

Fig. 4. Spectrum of the MIM waveguide for $\epsilon_m = -143.497$ and $2a = \lambda/4$ where $\lambda = 1550$ nm is the wavelength of operation. There are four real modes and an infinite number of complex modes, all denoted with the ● symbol. The thick line denotes the continuous spectrum. Due to the fact that ϵ_m is real, complex modes come in complex conjugate pairs. Insets show the H_y mode shapes in the x direction for the discrete spectrum (TM_0 through TM_8) and the continuous spectrum (TM_{C1} and TM_{C2})—solid lines in the insets are the real part of the mode, dashed lines are the imaginary part. The locations of the drawn continuous modes are shown by the ● symbol. Modes in the continuous spectrum are purely oscillatory in the x direction. Complex modes have a small decay, which is not visually apparent in the inset for TM_8.

point spectrum splits into two branches that are complex conjugates of one another. $\kappa_m^2 = 0$ corresponds to $k_z^2 = \epsilon_m k_0^2$ which then implies $k_z = -i\sqrt{|\epsilon_m|}k_0$—bounded modes should have $\mathrm{Im}(k_z) < 0$.

When loss is introduced to the metal, the spectrum moves on the complex plane.[42] The forward, proper, complex modes of the lossless case turn into leaky modes by migrating into the third quadrant of the complex κ_m plane.

4.3. Discretization of the Continuous Spectrum

The presence of a continuous spectrum leads to the formation of integral equations when the mode-matching method is applied.[48] The integral equation is then expanded using an orthogonal basis set—not necessarily that of the modes—to solve the scattering problem.

Another way to approach the scattering problem is to limit the transverse coordinates by a PEC wall. This approach has the effect of discretizing the continuum part of the spectrum[47, 60]—turning it into a discrete spectrum. To limit parasitic reflections from the PEC walls, absorbing layers can be positioned before the PEC termination.[38] In Ref. [61] detailed analysis of how the continuous spectrum appears from a discrete collection can be found. We will use a PEC wall to discretize the continuous spectrum. Also, we will not use any perfectly matched layers to limit parasitic reflections since the metallic sections with permittivity ϵ_m effectively absorb the fields away from the junction.

The geometry is as shown in Figure 3(b). For the left waveguide the dispersion equation for modes becomes

$$\tanh(\kappa_{i,n}a) = -\frac{\kappa_{m,n}/\epsilon_m}{\kappa_{i,n}/\epsilon_i}\tanh(\kappa_{m,n}h) \tag{29}$$

which asymptotes to (22) as $h \to \infty$. The transverse magnetic field shape is

$$\psi_n(x) = H_0 \begin{cases} \dfrac{\cosh(\kappa_{i,n}x)}{\cosh(\kappa_{i,n}a)} & 0 < x < a \\ \dfrac{\cosh(\kappa_{m,n}(x-a-h))}{\cosh(\kappa_{m,n}h)} & a < x < a+h \end{cases} \tag{30}$$

4.4. Mode Completeness

We tested the completeness of the modes by expanding the fundamental mode of an MIM waveguide of a given thickness in terms of the modes of the MIM waveguide with a different thickness. Without the continuous spectrum, the field expansion converges, but to a field profile which is not the same as the desired profile of the right junction.[42] On the other hand, inclusion of the continuous spectrum through the discretization of the continuum by a PEC wall leads to the correct field profile. Similarly, we found that for the magnetic field profile at the junction of two MIM waveguides convergence of the fields on both sides of the junction is obtained only when the continuous spectrum is also taken into consideration. Thus, it is clear that the point spectrum on its own is not sufficient to describe the behavior of the waveguide junctions. Inclusion of the continuous spectrum is essential. This is further illustrated in the next section.

4.5. Convergence of the Mode-Matching Method

Now that we know how to treat the continuous spectrum and are confident that the collection of the point and the continuous spectrum results in a complete basis set, we can proceed with the mode-matching formalism. We will begin by assuming that the pth mode of the left waveguide propagates toward the right, scatters and creates the following set of fields at the right and left sides of the junction, which by the continuity of the tangential magnetic and electric fields, are set equal

$$\sum_{m=1}^{\infty}(\delta_{mp} + R_{mp})h_L^{(m)}(x) = \sum_{k=1}^{\infty} T_{kp}h_R^{(k)}(x) \tag{31}$$

$$\sum_{m=1}^{\infty}(\delta_{mp} - R_{mp})e_L^{(m)}(x) = \sum_{k=1}^{\infty} T_{kp}e_R^{(k)}(x) \tag{32}$$

Here R_{mp} is the reflection coefficient of the mth mode of the left waveguide in response to an incoming field in the pth mode. Similarly, T_{kp} is the transmission coefficient of the kth mode of the right waveguide. Note that we chose R_{mp} to denote the reflection coefficient for the transverse magnetic fields, which automatically results in $-R_{mp}$ as the reflection coefficient for the transverse electric fields.

In Ref. [62], it is shown that the testing of the above equations (i.e., the discretization of the equation using integration of both sides by a given function) should be done by the magnetic field of the larger waveguide for enforcing electric field continuity (32) and by the electric field of the smaller waveguide to enforce the magnetic field continuity (31). Although that analysis was specifically done for waveguides with perfect metals ($|\epsilon_m| \to \infty$), we still use that strategy so that the formulation limits to the correct one should metals be made perfect.

For those cases where $a < a'$, we will take the pseudo-inner product of (31) with $e_L^{(n)}$ and of (32) with $h_R^{(n)}$. Furthermore, assuming there are L modes on the left and R modes on the right, we get

$$\sum_{m=1}^{L}(\delta_{mp} + R_{mp})\Omega_L^{(m)}\delta_{mn} = \sum_{k=1}^{R} T_{kp}[e_L^{(n)} \mid h_R^{(k)}]$$

$$\sum_{m=1}^{L}(\delta_{mp} - R_{mp})[e_L^{(m)} \mid h_R^{(n)}] = \sum_{k=1}^{R} T_{kp}\Omega_R^{(k)}\delta_{kn}$$

with the help of (28). These are linear matrix equations with R_{mp} and T_{kp} as the unknowns. After calculating the inner products, the set of equations can be inverted to

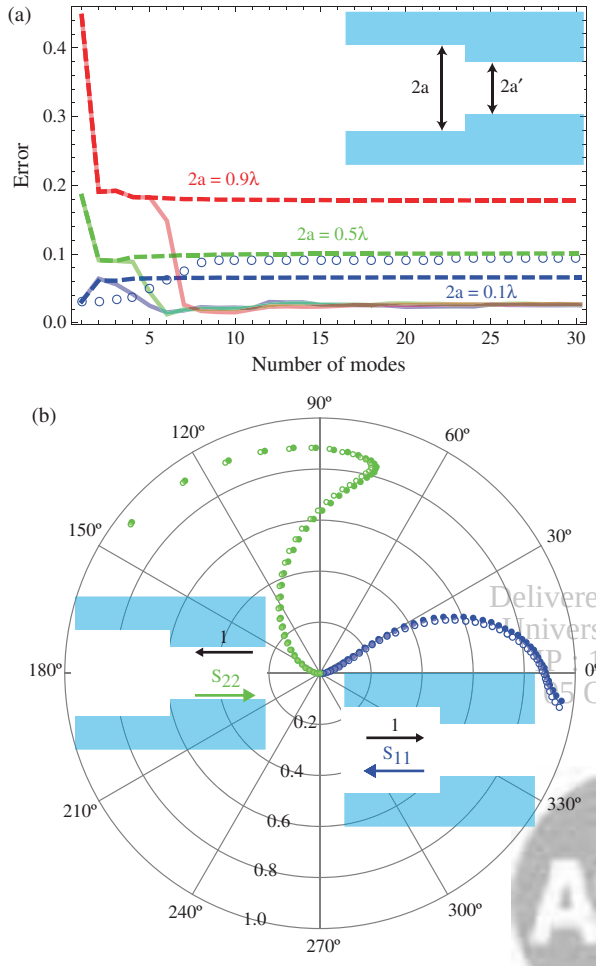

Fig. 5. (a) Convergence study of the reflection coefficient, S_{11}, of the main mode of the left waveguide traveling toward the right waveguide for $2a = 0.9\lambda$, $2a = 0.5\lambda$ and $2a = 0.1\lambda$. $a'/a = 0.4$ and $\epsilon_m = -143.497 - i9.517$ for all cases. Dashed lines are for calculations including the point spectrum only. Solid lines are those with both the point and the continuous spectrum. Empty circles denote the calculations done with the forward point spectrum and the continuous spectrum for the $2a = 0.1\lambda$ case only. Error is defined as $|(S_{11}^{MM} - S_{11}^{FDFD})/S_{11}^{FDFD}|$ where MM stands for mode-matching and FDFD for finite-difference frequency-domain calculations. The inset shows the junction geometry. (b) Reflection coefficient of the main mode at the junction between two MIM waveguides of different insulator thicknesses, plotted on the complex plane within the unit circle. Both waveguides have $\epsilon_m = -143.497 - i9.517$ and $\epsilon_i = 1.0$. Filled circles, •, are FDFD results, empty circles, ∘, are mode-matching results. The left waveguide thickness is fixed at $2a = 0.9\lambda$. The right waveguide thickness varies from $2a' = \{0.02\lambda, 0.04\lambda, \ldots, 0.9\lambda\}$. The origin is the zero reflection point that corresponds to $a = a'$. As a' decreases progressively toward zero, we move progressively along the curves away from the origin. The first set of curves, S_{11}, are for the case when the mode of the left waveguide, traveling from left to right, is scattered by the junction. The second set of curves, S_{22}, are for the case when the main mode of the right waveguide, traveling from right to left, is scattered by the junction. Insets illustrate the respective cases.

give the reflection and transmission coefficients for the modes.

In Figure 5(a), we compare the mode-matching method with the FDFD technique. It takes relatively few modes for the mode-matching calculations to converge. Without the continuous spectrum, the mode matching results converge to the wrong result. Inclusion of the continuous spectrum decreases the error to around 2%, which is probably due to the space discretization of FDFD simulations as well as the method used in the de-embedding of the scattering coefficients from fields. As is also evident from Figure 5(a) the utility of the single mode ($L = R = 1$) mode-matching calculations increases as the dimensions of the waveguides decreases. The single mode approximation is closely related to the characteristic impedance model described in Section 5.1 which is a good approximation for deep subwavelength structures. In Figure 5(a) we also show the effect of neglecting the backward modes in the mode-matching calculations for the $2a = 0.1\lambda$ case. Backward modes are important in this subwavelength geometry; however, for the wider geometries of the $2a = 0.5\lambda$ and $2a = 0.9\lambda$ cases we did not observe any increase in the error when backward modes were neglected in the mode-matching calculations.

In Figure 5(b) we visualize the scattering coefficient of the main mode of the MIM waveguide. (The extraction of the scattering parameters from full field simulations is described in detail in the section below.) We do the calculations in two different ways, one using FDFD, and the other using the mode-matching technique with the point and the continuous spectrum. When applying mode-matching, we use the $a > a'$ formulation for S_{11} calculations and the $a < a'$ one for S_{22}. There is a very good match between the results of the two techniques, verifying the applicability of the mode-matching method. In addition, since the convergence of the mode-matching method requires relatively few modes, the use of the mode-matching technique results in orders of magnitude speedup in the calculation of the properties of the junction.

5. EQUIVALENT MODELS FOR PLASMONIC WAVEGUIDE COMPONENTS

Modeling electromagnetic wave propagation using transmission lines has been one of the most important achievements of microwave network theory.[63] The concept of impedance[64] and understanding the effects of waveguide discontinuities in terms of lumped circuit elements were crucial in this respect. Even though the properties of metals are quite different at optical wavelengths compared to the microwave, designs that are qualitatively similar to their low frequency counterparts have been demonstrated at optical frequencies.[65] It has also been shown that the fundamental TM mode of an MIM waveguide continuously changes to the TEM mode of a parallel-plate waveguide with PEC boundaries as the frequency of operation is decreased.[66] It is intriguing to ask whether methods of microwave can be applied to this new generation of nanometallic structures to come up with concise descriptions of

components that can lead to a simplified approach to the design of functional systems composed of many interacting parts.

Here we first introduce the concept of the characteristic impedance for MIM plasmonic waveguides and we show its validity and usefulness for subwavelength guides. We then characterize the modal reflection and transmission from MIM junctions using the scattering matrix approach, a commonly used method in microwave network theory. We also represent the scattering matrix of MIM junctions in terms of an equivalent lumped circuit model. Finally, to test our characterization, we design a cascade connection of MIM junctions to couple the mode of a wavelength-sized MIM waveguide to that of a subwavelength one with zero reflection. Throughout our analysis, we will compare MIM waveguides to PEC parallel plate waveguides and comment on the similarities and the differences between the two.

5.1. Characteristic Impedance Model

The characteristic impedance of the fundamental TEM mode in a PEC parallel-plate waveguide is uniquely defined as the ratio of voltage V to surface current density I and is equal to[67]

$$Z_{\mathrm{TEM}} \equiv \frac{V}{I} = \frac{E_x d}{H_y} = \frac{\beta_{\mathrm{TEM}}}{\omega \epsilon_0} d = \sqrt{\frac{\mu_0}{\epsilon_0}} d \tag{33}$$

where E_x, H_y are the transverse components of the electric and magnetic field respectively, and we assumed a unit-length waveguide in the y direction. For non-TEM modes, such as the fundamental MIM mode, voltage and current are not uniquely defined. However, metals like silver satisfy the condition $|\epsilon_{\mathrm{metal}}| \gg \epsilon_{\mathrm{diel}}$ at the optical communication wavelength of 1.55 μm.[27] Thus, $|E_{x\,\mathrm{metal}}| \ll |E_{x\,\mathrm{diel}}|$ so that the integral of the electric field in the transverse direction can be approximated by $E_{x\,\mathrm{diel}}\, d$ and we may therefore define the characteristic impedance of the fundamental MIM mode as[15]

$$Z_{\mathrm{MIM}}(d) \equiv \frac{E_{x\,\mathrm{diel}}\, d}{H_{y\,\mathrm{diel}}} = \frac{\beta_{\mathrm{MIM}}(d)}{\omega \epsilon_0} d \tag{34}$$

where $\beta_{\mathrm{MIM}}(d) = 2\pi/\lambda_g(d)$, and λ_g is the guide wavelength. In Figure 6 we show the reflection coefficient of an MIM T-shaped splitter calculated based on Z_{MIM} as

$$\bar{R} = \left| \frac{Z_{\mathrm{L}} - Z_0}{Z_{\mathrm{L}} + Z_0} \right|^2 = \left| \frac{2Z_{\mathrm{MIM}}(d_{\mathrm{out}}) - Z_{\mathrm{MIM}}(d_{\mathrm{in}})}{2Z_{\mathrm{MIM}}(d_{\mathrm{out}}) + Z_{\mathrm{MIM}}(d_{\mathrm{in}})} \right|^2 \tag{35}$$

We observe that there is very good agreement between $\bar{R}$ and the exact reflection coefficient R calculated using FDFD. This agreement suggests that the concept of characteristic impedance for MIM waveguides is indeed valid and useful. The deviation between $\bar{R}$ and R at large values of $d_{\mathrm{in}}/d_{\mathrm{out}}$ is due to the fact that d_{in} is not very small compared to the wavelength and the quasistatic approximation therefore breaks down. We found that similar deviations are observed for PEC parallel-plate waveguides. Such deviations decrease at longer wavelengths in both the PEC and MIM waveguide cases.

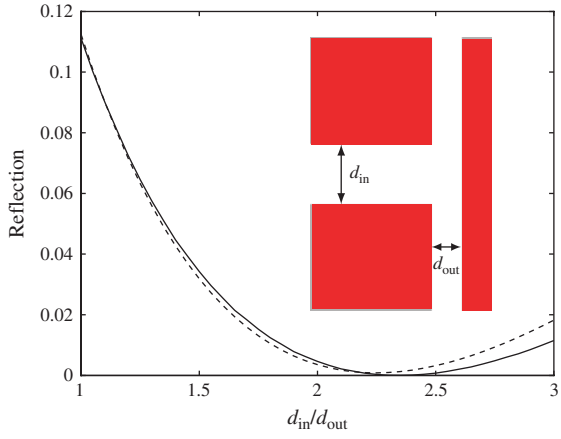

Fig. 6. Reflection coefficient R of a MIM T-shaped splitter (shown in the inset) as a function of $d_{\mathrm{in}}/d_{\mathrm{out}}$ at $\lambda_0 = 1.55$ μm calculated using FDFD. We also show with dashed line the reflection coefficient $\bar{R}$ calculated based on the characteristic impedance Z_{MIM} and transmission-line theory. Results are shown for $d_{\mathrm{out}} = 50$ nm.

5.2. Scattering Matrix Description of Junctions

In this section, we characterize the modal reflection and transmission from MIM junctions using the scattering matrix approach, a commonly used method in microwave network theory.[68] We consider the geometry shown in Figure 7(a). The insulating region is free space with a permittivity $\epsilon_i = 1$, and the metal is silver with a permittivity of $\epsilon_m = -143.497 - i9.517$.[27,59] The wavelength of operation is fixed at $\lambda = 1550$ nm, in the L band of optical telecommunications.

Using the dispersion equation for even modes of the MIM waveguide it can be shown that only a single even propagating mode can exist for $2a < 0.97\lambda$ for our choice of ϵ_m, ϵ_i and λ. The condition for the PEC parallel plate waveguide is similar, where only a single even propagation mode exists for $2a < 1.0\lambda$. When there is only one propagating mode, far away from the waveguide junction the fields can be written in terms of that main mode of the system since all higher order modes will have an exponential decay much faster compared to the main propagating mode. Under such circumstances, the effects of the waveguide junction on the propagating modes can be described using the single mode *scattering matrix* (**S**) formalism.[69] In the terminology of the scattering matrix, the forward and backward mode amplitudes are considered to scatter from one "port" to another. Here we can think of the ports as being the left and right port planes shown in Figure 7(a). These ports are sufficiently far to the left and right of the junction that the fields have settled down again to being

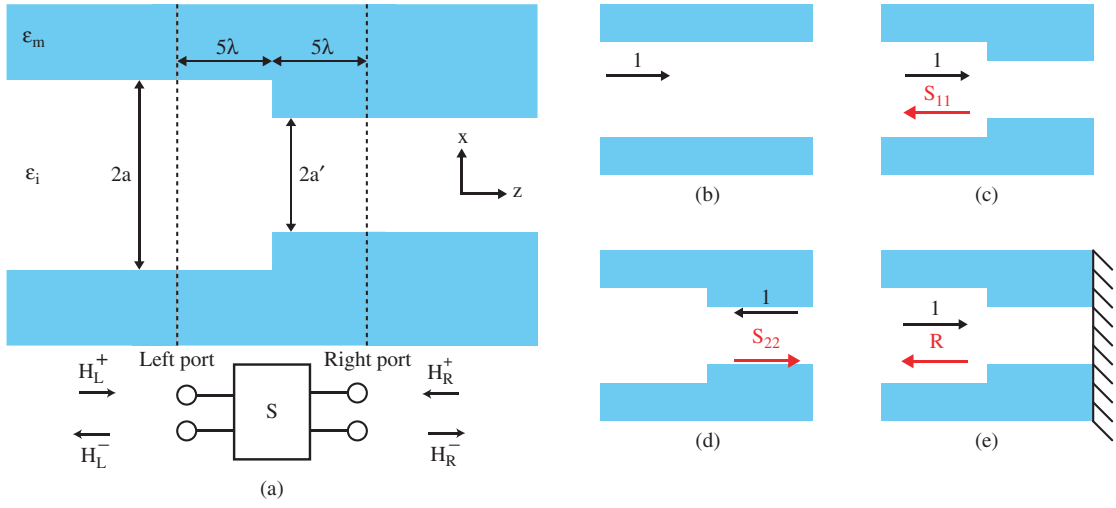

Fig. 7. (a) Description of the modeling geometry. Dashed lines represent the location of the left and right ports of the overall scattering matrix **S** that describes this junction (schematically shown in the bottom part of the figure). (b) Description of the steps taken in extracting **S** from fields. Calibration simulations with uniform insulator widths of $2a$ and $2a'$, which give the wave vector k and the values of the incoming fields at the left, $H_L^+\psi_L(x)$, and right ports, $H_R^+\psi_R(x)$. (c) Field impinging from the left side, which leads to S_{11}. (d) Field impinging from the right side, which leads to S_{22}. (e) Simulation domain is terminated by a perfect electric conductor at the right input port plane. S_{12} is extracted from the reflection coefficient R using the previously calculated S_{11} and S_{22}.

the propagating modes of the guides (nearer to the interface, there will in general be other field behavior, including various near-field components that decay rapidly with distance).

If we can deduce the scattering matrix for such a junction, then we can have a very simple way of modeling the behavior of structures containing such junctions, as is already well known in the modeling of microwave guides. The elements of the scattering matrix, S_{11}, S_{12}, S_{21}, S_{22}, are complex numbers which describe the phase and magnitude of the reflection and transmission of the main modes. Thus, in general there are 8 independent real numbers in **S**. However, under certain conditions the number of independent parameters can be reduced. First of all, if the system is composed of reciprocal media (i.e., symmetric permittivity and permeability tensors) then using the Lorentz reciprocity theorem it can be shown that $S_{12} = S_{21}$. Note that this equality implies a certain normalization of the modes,[69] specifically

$$\int_{\mathbf{A}} \mathbf{E}_L \times \mathbf{H}_L \cdot d\mathbf{A} = \int_{\mathbf{A}} \mathbf{E}_R \times \mathbf{H}_R \cdot d\mathbf{A} = 1 \qquad (36)$$

where $\mathbf{E}_{\{L,R\}}$ and $\mathbf{H}_{\{L,R\}}$ denote the electric and magnetic components of the main propagating modes on the left (L) and the right (R) of the waveguide junction. Also note that for lossless systems **S** is a unitary matrix[69] (though in general here we will be considering systems with loss). As a result, using reciprocity it is possible to describe a lossy junction using six real numbers, two for each of S_{11}, S_{12}, and S_{22}. When there is no loss we only need three real numbers due to the unitarity of **S**.

We now describe the method we used to extract the elements of **S** from the electromagnetic fields in such waveguide junctions. We solved Maxwell's equations using the FDFD method. In the vicinity of the waveguide junction, higher order modes will be excited. We chose the left and right ports of our junction sufficiently (5λ) away from the physical junction where the amplitudes of the higher order modes are negligible. In the following we will formulate **S** in terms of the transverse magnetic field component H_y. We will use $\psi_L(x)$ to denote the main mode of the left waveguide and $\psi_R(x)$ for the right waveguide.

The scattering matrix relates the amplitudes and phases of the modes that arrive at the left and right ports, H_L^+, H_R^+ to the amplitudes and phases of the modes that propagate away from the ports, H_L^- and H_R^-. Formally we can write

$$\begin{pmatrix} H_L^- \\ H_R^- \end{pmatrix} = \begin{pmatrix} S_{11} & S_{12} \\ S_{21} & S_{22} \end{pmatrix} \begin{pmatrix} H_L^+ \\ H_R^+ \end{pmatrix} \qquad (37)$$

In order to extract **S** we need to know the fields that arrive at the left and right ports from our numerical sources in the simulation domain. To do that we do two calibration simulations (one for the left waveguide, another for the right waveguide) without any discontinuities, as shown in Figure 7(b), and record the fields. This gives us the required $H_{\{L,R\}}^+\psi_{\{L,R\}}(x)$ in addition to the propagation vectors, $k_{\{L,R\}}$, of the two main modes for guides of insulator thicknesses $2a$ and $2a'$ respectively. Then we do two more simulations where we send the mode from the left and from the right waveguide to the discontinuity as schematically shown in Figures 7(c–e). From the results of the simulation in Figure 7(c), for the fields to the left of the left port, $H_L(x,z)$, we get

$$\begin{aligned} H_L(x,z) &= [H_L^+ e^{-ik_L z} + H_L^- e^{+ik_L z}]\psi_L(x) \\ &= [H_L^+ (e^{-ik_L z} + S_{11} e^{+ik_L z})]\psi_L(x) \end{aligned}$$

where the location of the left port determines the origin for z and in (37) we used the fact that $H_R^+ = 0$ for the simulation depicted in Figure 7(c). Simple algebra gives

$$S_{11} = \frac{H_L(x,z)}{H_L^+ \psi_L(x)} e^{-ik_L z} - e^{-2ik_L z} \tag{38}$$

Very similarly, we also extract S_{22} from the results of the simulation of Figure 7(d).

In order to extract S_{12}, we terminate our simulation domain at the plane of the right port with a perfect electric conductor. Such a termination results in zero tangential electric fields and therefore gives -1 for the reflection coefficient of the transverse electric field, E_x, and $+1$ for the magnetic field, H_y. Thus, at the right port we get $H_R^- = H_R^+$. Using this equality in (37), we get the reflection coefficient, $R = H_L^-/H_L^+$, in Figure 7(e)

$$R = S_{11} + \frac{S_{12}S_{21}}{1 - S_{22}} = S_{11} + \frac{S_{12}^2}{1 - S_{22}} \tag{39}$$

where in the last equality we used the fact that $S_{21} = S_{12}$. We extract R using the same method as we used in the extraction of S_{11}. From the knowledge of R, S_{11} and S_{22} one can easily invert (39) to calculate S_{12}.

After we calculate $\mathbf{S}$ for the ports defined in Figure 7(a), we shift both the left and right reference planes back to the exact location of the junction using

$$\mathbf{S}_J = \begin{pmatrix} e^{ik_L\ell_L} & 0 \\ 0 & e^{ik_R\ell_R} \end{pmatrix} \mathbf{S} \begin{pmatrix} e^{ik_L\ell_L} & 0 \\ 0 & e^{ik_R\ell_R} \end{pmatrix} \tag{40}$$

where $\ell_L = \ell_R = 5\lambda$ as defined in Figure 7(a) and $\mathbf{S}_J$ is the effective scattering matrix for the case where the left and right ports are projected back to coincide with the junction plane.[69] For the sake of notational abbreviation, from this point on we will use $\mathbf{S}$ to imply $\mathbf{S}_J$. Note that this effective scattering matrix is defined just for the algebraic convenience of having a scattering matrix associated directly with the position of the interface. The fields near to the interface are not in fact just describable by these single main modes because of various near field effects of higher order modes.

Note that the polar plot of the reflection coefficients is nothing other than the Smith chart of the microwave theory,[70] which we will use in Section 5.4.

5.3. Circuit Model for the Waveguide Junction

Another important approach in microwave waveguide modeling is the use of equivalent circuit models, which can give an intuitive picture of the system as well as allowing the use of circuit simulators for design.

Here we relate the scattering matrix to simplified circuit models that can characterize the MIM waveguide interfaces. Since we only have single propagating modes in the guides we consider, we can also use equivalent transmission lines to describe the propagation between interfaces. Taking these circuit and transmission line approaches together, we can then model a broad range of MIM systems with circuit models.

There is no unique way to describe $\mathbf{S}$ using lumped circuit elements.[71] To choose one circuit out of the infinite possible set that could correspond to the same $\mathbf{S}$, we will first look at the well studied PEC case. The solution to the scattering problem for the junction of two PEC parallel plate waveguides was developed and experimentally verified.[72] It consists of a capacitor with susceptance B and a transformer with a turns ratio of n:1. The susceptance and the turns ratio are described in terms of the geometry of the junction. The square of the turns ratio of the transformer is equal to

$$n^2 = \frac{a'}{a} \tag{41}$$

It is worthwhile remembering that the primary-secondary turns ratio of the transformer, n:1, is also the ratio of the voltages at its terminals. From the conservation of power, currents have the inverse ratio and as a result the impedance ratio at the transformer terminals is n^2:1. The derivation of the circuit elements for the PEC case can be found in Refs. [73–75]. Note that for the PEC case, only two parameters, B and n, are sufficient to describe the junction even though in general three parameters are required for a lossless reciprocal system. The nondispersive nature of the main mode of PEC parallel plate waveguides leads to a further symmetry in the junction which reduces the number of circuit parameters required.

At optical frequencies where the modes are strongly dispersive, a third circuit element is needed in order to be able to fit the elements of $\mathbf{S}$ exactly. For that reason we have an inductor term with a reactance X. A schematic of the circuit diagram is shown in Figure 8(a). The PEC parallel plate waveguide circuit is the same, with $X = 0$. The normalization that we defined in (36) leads to transmission lines with a unit characteristic impedance on both sides of the junction. From transmission line theory we get the following equalities in terms of the equivalent impedance looking from the left side of the circuit, Z_1, and the equivalent admittance looking from the right side, Y_2

$$-S_{11} = \frac{Z_1 - 1}{Z_1 + 1} \quad \text{and} \quad -S_{22} = \frac{1 - Y_2}{1 + Y_2} \tag{42}$$

where

$$\begin{aligned} Z_1 &= iX + \frac{1}{iB + (1/n^2)} \\ Y_2 &= \left(\frac{1}{1 + iX} + iB \right) n^2 \end{aligned} \tag{43}$$

The reason why we have negative signs in front of S_{11} and S_{22} in (42) is because we defined $\mathbf{S}$ based on the transverse magnetic component of the main mode, H_y. However, the norm in circuit parametrization is to use the voltage reflection and transmission coefficients, which correspond to

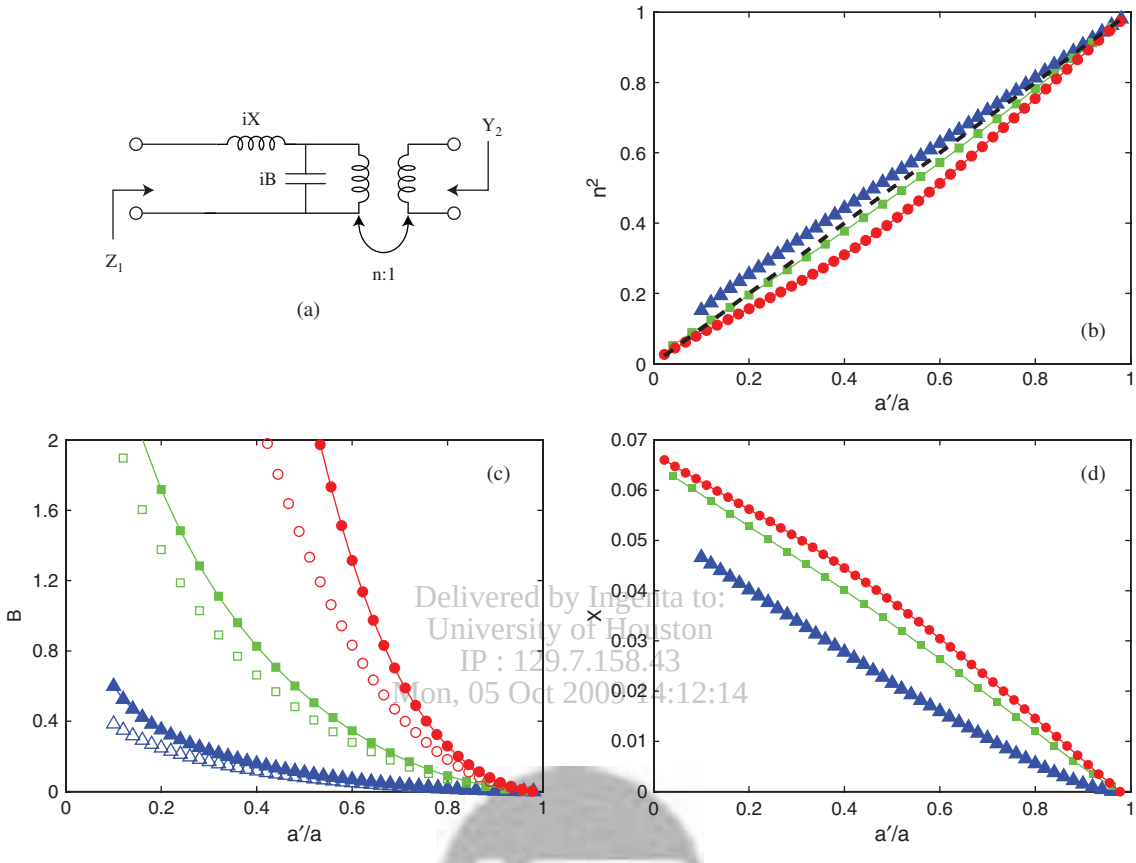

Fig. 8. (a) Circuit description of the lossless ($\epsilon_m = -143.497$) waveguide junction for $2a = 0.1\lambda$ (▲), $2a = 0.5\lambda$ (■), $2a = 0.9\lambda$ (●). (b) Square of the turns ratio, n^2, which is equivalent to the impedance ratio at the terminals of the transformer. Dashed line is the PEC result described by (41). (c) Susceptance, B, for the MIM (▲, ■, ●) and the PEC (△, □, ○) case. (d) Reactance, X, of the MIM waveguide. $X = 0$ for the PEC parallel plate waveguide.

a scattering matrix description for the transverse electric component, E_x. Just as in transmission line theory where the reflection coefficient for voltage is the negative of that of the current, the same relationship also holds exactly between the reflection coefficients of E_x and H_y.

Let the real and imaginary parts of Z_1 and Y_2 be denoted as $Z_R = \mathrm{Re}(Z_1)$, $Z_I = \mathrm{Im}(Z_1)$, $Y_R = \mathrm{Re}(Y_2)$ and $Y_I = \mathrm{Im}(Y_2)$. Using (43) we get

$$Bn^2 = \frac{Y_I + Y_R Z_I}{1 - Y_R Z_R} \quad \text{and} \quad X = \frac{Z_I + Z_R Y_I}{1 - Y_R Z_R} \tag{44}$$

Once we know Bn^2 and X, we can calculate n^2 using (43) as

$$n^2 = Y_R(1 + X^2) = Z_R\left[1 + (Bn^2)^2\right] \tag{45}$$

Using Eqs. (42), (44) and (45) one can calculate the circuit parameters from S_{11} and S_{22}. In Figures 8(b–d) we plotted n^2, B and X as a function of a'/a for the three different fixed $2a$ values of 0.1λ, 0.5λ and 0.9λ. It can be seen that the PEC circuit description and the MIM circuit description lead to parameters which qualitatively have similar behaviors.

5.4. Cascade Connection of Junctions

We now test the utility of the scattering matrix description by numerically simulating mode propagation through a cascade connection of junctions and comparing the results with the predictions of the scattering matrix formalism.

When different scattering matrices are cascaded, the *transfer matrix*, **T**, leads to a much simpler formulation[76]

$$\begin{pmatrix} H_L^+ \\ H_L^- \end{pmatrix} = \begin{pmatrix} T_{11} & T_{12} \\ T_{21} & T_{22} \end{pmatrix} \begin{pmatrix} H_R^- \\ H_R^+ \end{pmatrix} \tag{46}$$

5.4.1. Conditions for Zero Reflection

In order to have $H_L^- = 0$, one should have $T_{21}H_R^- + T_{22}H_R^+ = 0$, which can be cast in terms of the scattering parameters as

$$S_{11}H_R^- = (S_{11}S_{22} - S_{12}S_{21})H_R^+ \tag{47}$$

a. Lossy Case. Let us investigate the case when two junctions characterized by two different scattering matrices, ${}^L\mathbf{S}$ and ${}^R\mathbf{S}$, are separated by a center waveguide of length ℓ as shown in Figure 9(a). Suppose that we adjust

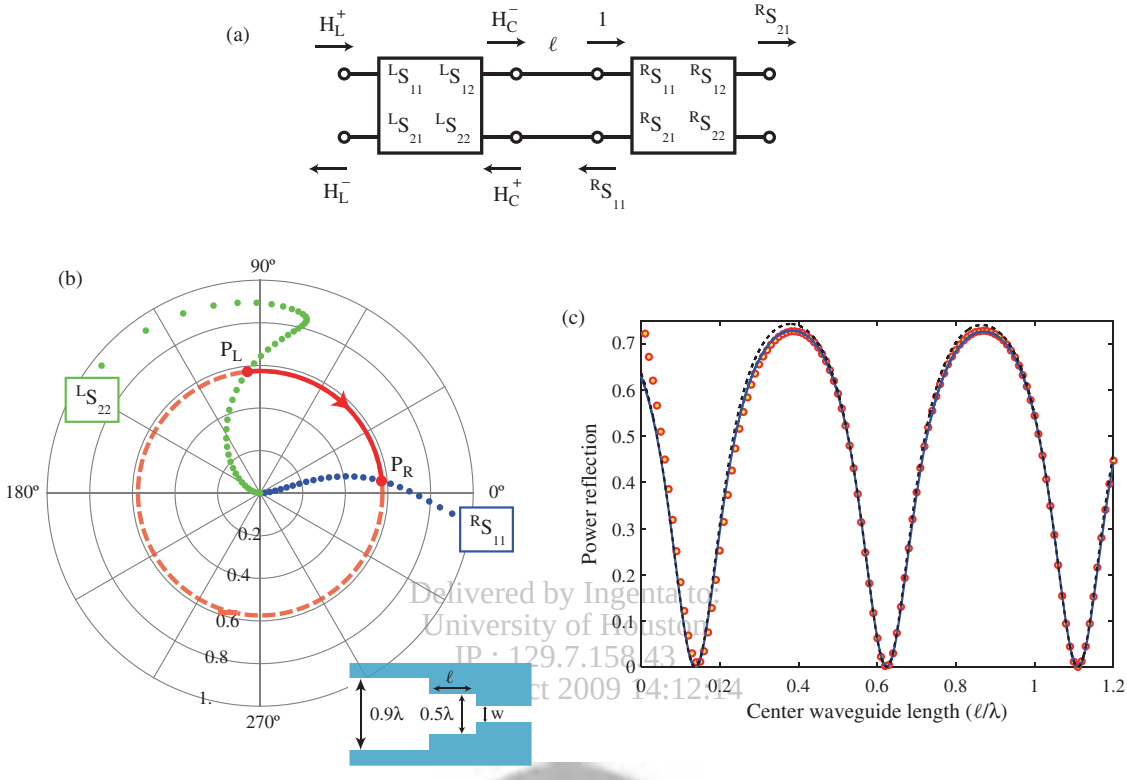

Fig. 9. (a) Schematic diagram of modal propagation. The left and right junctions are shown as boxes with an **S** matrix description. The center waveguide is shown as a transmission line of length ℓ. The source that creates the fields is normalized such that the mode that propagates to the right has a unit magnitude at the input of the right junction. (b) Graphical solution of (50) and (51) on the complex plane. Point P_L is the location of the left junction on the $^LS_{22}$ curve where $2a = 0.9\lambda$ and $2a' = 0.5\lambda$. Point P_R is the location of the right junction on the $^RS_{11}$ curve where $2a = 0.5\lambda$ and $2a' = 0.16\lambda$. (c) Test of the scattering matrix description. Horizontal axis is the length of the center waveguide normalized to λ. Vertical axis is the power reflection coefficient. FDFD simulation results (•), transfer matrix calculations using lossy junctions (solid line) and lossless junctions (dashed line) are also plotted. Transfer matrix calculations do take into account the loss in the center waveguide for both cases. As the junctions get very close to each other (<0.1λ) transfer matrix model begins to break down due to higher order modal interactions.

our excitation amplitude such that the mode that propagates toward the right junction at its input plane, which is the junction plane, has unit strength. That choice of normalization leads to $H_R^- = e^{ik_C\ell}$ and $H_R^+ = {}^RS_{11}e^{-ik_C\ell}$ where k_C is the wave vector of the center waveguide. With these definitions, the condition for zero reflection, (47), for the left junction can be written as

$$e^{-2ik_C\ell} = \frac{{}^LS_{11}/{}^RS_{11}}{{}^LS_{11}{}^LS_{22} - {}^LS_{12}{}^LS_{21}}$$

For reciprocal media, $S_{12} = S_{21}$, we can write

$$e^{-2ik_C\ell} = \frac{{}^LS_{11}/{}^RS_{11}}{{}^LS_{11}{}^LS_{22} - {}^LS_{21}^2} \quad (48)$$

b. Lossless Case. If the system is lossless, then the scattering matrix should be unitary ($\mathbf{SS}^\dagger = \mathbf{1}$) which implies the following three conditions

$$|S_{11}|^2 = |S_{22}|^2 = 1 - |S_{12}|^2$$
$$\frac{S_{12}}{S_{21}^*} = -\frac{S_{22}}{S_{11}^*} \quad (49)$$

Using (48) and (49), the zero reflection condition becomes

$$|{}^LS_{22}| = |{}^RS_{11}| \quad \text{(magnitude condition)} \quad (50)$$

$$\measuredangle{}^LS_{22} + \measuredangle{}^RS_{11} = 2k_C\ell + 2\pi n \quad \text{(phase condition)} \quad (51)$$

where n is any integer value, superscripts R and L denote right and left respectively. "$\measuredangle$" is used to represent the argument of a complex number. What this means is that, to match a left waveguide to a right waveguide, one should choose a center waveguide width which satisfies the magnitude condition, and decide on the length of the center waveguide based on the phase condition.

Once a matching left, center and right waveguide triplet is found, the procedure can be recursively repeated to cascade more junctions without getting any reflection at the leftmost waveguide.

5.4.2. Mode Converter Design

Now that we have the conditions (48) and (50–51) for zero reflection, we can test their validity. Condition (48) is more general and is applicable to the lossy case. We did a series of simulations in which we extracted **S** for a hypothetical lossless metal with a real, negative permittivity $\epsilon_m = -143.497$. The results were very similar to the case

where the loss was included. That led us to suspect that the conditions for the lossless reciprocal junctions, (50) and (51), would be essentially sufficient in the design of a mode converter that converts the mode of a wavelength sized MIM waveguide ($2a = 0.9\lambda$) to that of a subwavelength one with no reflection.

In our design we choose the left waveguide width to be 0.9λ and the center waveguide width to be 0.5λ as shown in the inset in Figure 9(b). The parameters that we need are the insulator width of the right waveguide, w, and the length of the center waveguide, ℓ.

The width of the right waveguide can be chosen by satisfying (50). In Figure 9(b) P_L is the location of the $2a = 0.9\lambda$ to $2a' = 0.5\lambda$ junction on the ${}^{L}S_{22}$ curve. To satisfy (50) we need to have $|{}^{L}S_{22}| = |{}^{R}S_{11}|$. The solution can be graphically found by drawing a circle in the complex plane with a radius $|P_L|$ centered at the origin and finding its intersection with the ${}^{R}S_{11}$ curve. The intersection point is denoted by P_R. P_R corresponds to a right waveguide thickness of 0.16λ. The phase condition (51) is then easily calculated from the phases of the scattering coefficients, $\angle P_L$ and $\angle P_R$. After some simplification through the use of the numerical value for k_C one gets $\ell/\lambda = 0.1377 + 0.4861n$, where n is any positive integer.

To check our design, we numerically simulated the structure shown in the inset of Figure 9(b) using FDFD and looked at the amount of power reflected back as a function of the center waveguide length ℓ. We also calculated the power reflection coefficient through the use of the transfer matrix formalism in which we multiplied the transfer matrices for the right junction, $\mathbf{T}_R$, a center waveguide of length ℓ, $\mathbf{T}_C$, and the left junction, $\mathbf{T}_L$, to get the overall transfer matrix $\mathbf{T} = \mathbf{T}_L\mathbf{T}_C\mathbf{T}_R$, and plotted $|T_{21}/T_{11}|^2$ of $\mathbf{T}$ as a function of ℓ/λ. We did the calculations for two different sets of $\{\mathbf{T}_R, \mathbf{T}_L\}$: one in which we used the scattering matrices for the lossy junctions and another for the lossless junctions. The center waveguide of length ℓ had loss in both cases i.e., $k_C = (1.03 - i9.45 \times 10^{-4})2\pi/\lambda$.

Figure 9(c) verifies that lossless junction models are quite effective at modeling the waveguide discontinuities and the prediction of the length of the center guide for zero reflection reached by their use, $\ell/\lambda = 0.1377 + 0.4861n$ is very accurate. The lossy junction model on the other hand gives results essentially indistinguishable from the simulation results as long as the two junctions are not very close to each other ($< 0.1\lambda$). When the junctions get very close, the coupling of higher order non-propagating modes becomes important and the single mode modeling we employed in the construction of scattering matrices breaks down. For such closely spaced junctions, the whole structure should be treated as a single unit and its characteristics should be extracted by the techniques described in Section 5.2.

6. SUMMARY AND CONCLUSIONS

In this paper, we first gave an overview of the challenges involved in modeling of plasmonic devices, and briefly examined two general purpose simulation techniques which are widely used for modeling of plasmonic waveguide devices.

We then introduced the mode-matching technique for modeling of MIM waveguide devices. We derived the complete set of orthogonal modes that the MIM waveguide supports. We showed that in addition to the previously unreported complex set of discrete modes, there also exists a continuous set of modes. We then used the complete set of modes to apply the mode-matching technique in the investigation of modal scattering at the symmetric junction of two MIM waveguides with different cross sections.

This special purpose simulation technique is far more efficient for this class of problems than general purpose electromagnetic simulation techniques. The knowledge of the set of orthogonal modes which form a complete basis for a given geometry leads to a much more simplified algebra and speeds up calculations. These results are valuable for electromagnetic scattering calculations involving the MIM geometry. The analysis can also be generalized for other related geometries involving metals at optical frequencies.[77–81]

We also introduced several different equivalent models for plasmonic waveguide components. We first showed that the characteristic impedance model can accurately model the behavior of deep subwavelength MIM waveguides. We also extracted the scattering matrices of junctions of different geometries from full field solutions, and parametrized the scattering matrix of the MIM junction in terms of lumped circuit elements. We validated our characterization by designing a mode converter that concentrates light from an MIM waveguide of wavelength-sized dimension to one of subwavelength dimension with zero reflection.

The model abstraction provided by these equivalent models is important for the analysis and synthesis of device functions.[82–85] The circuit representation of the junction helps us associate the effects of geometry, material properties and wave propagation in terms of a simple network of a capacitor, inductor and a transformer. The scattering matrix description of junctions can be used to design optical circuitry with complex functionality using tools of circuit analysis.[86, 87] It is conceivable to build a library of junction geometries associated with their scattering matrices for different waveguides including three dimensional nano-metallic ones.[88] Such a library, indexed according to modal scattering and propagation properties, would be invaluable in the design of integrated optical circuits composed of many interacting components.

References

1. W. L. Barnes, A. Dereux, and T. W. Ebbesen, *Nature* 424, 824 **(2003)**.
2. E. Ozbay, *Science* 311, 189 **(2006)**.
3. J. Takahara, S. Yamagishi, H. Taki, A. Morimoto, and T. Kobayashi, *Opt. Lett.* 22, 475 **(1997)**.
4. J. C. Weeber, A. Dereux, C. Girard, J. R. Krenn, and J. P. Goudonnet, *Phys. Rev. B* 60, 9061 **(1999)**.
5. J. R. Krenn, B. Lamprecht, H. Ditlbacher, G. Schider, M. Salerno, A. Leitner, and F. R. Aussenegg, *Europhys. Lett.* 60, 663 **(2002)**.
6. M. L. Brongersma, J. W. Hartman, and H. A. Atwater, *Phys. Rev. B* 62, R16356 **(2000)**.
7. S. A. Maier, P. G. Kik, H. A. Atwater, S. Meltzer, E. Harel, B. E. Koel, and A. A. G. Requicha, *Nat. Mater.* 2, 229 **(2003)**.
8. S. I. Bozhevolnyi, V. S. Volkov, E. Devaux, and T. W. Ebbesen, *Phys. Rev. Lett.* 95, 046802 **(2005)**.
9. E. N. Economou, *Phys. Rev.* 182, 539 **(1969)**.
10. R. Zia, M. D. Selker, P. B. Catrysse, and M. L. Brongersma, *J. Opt. Soc. Am. A* 21, 2442 **(2004)**.
11. J. A. Dionne, L. A. Sweatlock, H. A. Atwater, and A. Polman, *Phys. Rev. B* 73, 035407 **(2006a)**.
12. E. Feigenbaum and M. Orenstein *Journal of Lightwave Technology* 25, 2547 **(2007a)**.
13. R. Gordon, *Phys. Rev. B* 73, 153405 **(2006)**.
14. Z. Han and S. He, *Opt. Commun.* 278, 199 **(2007)**.
15. G. Veronis and S. Fan, *Appl. Phys. Lett.* 87, 131102 **(2005)**.
16. K. Tanaka and M. Tanaka, *Appl. Phys. Lett.* 82, 1158 **(2003)**.
17. G. Veronis and S. Fan, *Opt. Express* 15, 1211 **(2007a)**.
18. P. Ginzburg and M. Orenstein, *Opt. Express* 15, 6762 **(2007)**.
19. J. A. Dionne, H. J. Lezec, and H. A. Atwater, *Nano Lett.* 6, 1928 **(2006b)**.
20. Y. Jiao, S. Fan, and D. Miller, *IEEE Journal of Quantum Electronics* 42, 266 **(2006)**.
21. W. Suh, Z. Wang, and S. Fan, *IEEE Journal of Quantum Electronics* 40, 1511 **(2004)**.
22. J. Bravo-Abad, S. Fan, S. G. Johnson, J. D. Joannopoulos, and M. Soljacic, *Journal of Lightwave Technology* 25, 2539 **(2007)**.
23. S. Fan, M. F. Yanik, Z. Wang, S. Sandhu, and M. L. Povinelli, *Journal of Lightwave Technology* 24, 4493 **(2006)**.
24. L. Novotny, B. Hecht, and D. Pohl *J. Appl. Phys.* 81, 1798 **(1997)**.
25. E. Prodan, P. Nordlander, and N. Halas, *Chem. Phys. Lett.* 368, 94 **(2003)**.
26. C. F. Bohren and D. R. Huffman, Absorption and Scattering of Light by Small Particles, Wiley Science, New York **(1983)**.
27. E. D. Palik, Handbook of Optical Constants of Solids, Academic, New York **(1985)**.
28. A. Taflove and S. C. Hagness, Computational Electrodynamics, Artech House, Boston **(2005)**.
29. A. D. Rakic, A. B. Djurisic, J. M. Elazar, and M. L. Majewski, *Appl. Opt.* 37, 5271 **(1998)**.
30. M. Han, R. Dutton, and S. Fan, *IEEE Microwave and Wireless Components Letters* 16, 119 **(2006)**.
31. A. Vial, A. Grimault, D. Macias, D. Barchiesi, and M. de la Chapelle, *Phys. Rev. B* 71, 85416 **(2005)**.
32. J. Jin, The Finite Element Method in Electromagnetics, John Wiley & Sons, New York **(2002)**.
33. P. Berini, *Phys. Rev. B* 61, 10484 **(2000)**.
34. G. Veronis, R. W. Dutton, and S. Fan, *Opt. Lett.* 29, 2288 **(2004)**.
35. J. Berenger, *J. Comput. Phys.* 114, 185 **(1994)**.
36. J. Young and R. Nelson, *IEEE Antennas and Propagation Magazine* 43, 61 **(2001)**.
37. P. J. B. Clarricoats and K. R. Slinn, *Proceedings of the Institution of Electrical Engineers* **(1967)**, Vol. 114, p. 878.
38. P. Bienstman, Ph.D. thesis, Ghent University, Belgium **(2001)**.
39. I. Breukelaar and P. Berini, *Journal of the Optical Society of America A* 23, 1971 **(2006)**.
40. I. Breukelaar, R. Charbonneau, and P. Berini, *J. Appl. Phys.* 100, 043104 **(2006)**.
41. R. F. Oulton, D. F. P. Pile, Y. Liu, and X. Zhang, *Phys. Rev. B* 76, 035408 **(2007)**.
42. Ş. E. Kocabaş, G. Veronis, D. A. B. Miller, and S. Fan, *Phys. Rev. B* 79, 035120 **(2009)**.
43. G. W. Hanson and A. B. Yakovlev, Operator Theory for Electromagnetics, Springer-Verlag, New York **(2002)**.
44. B. Prade, J. Y. Vinet, and A. Mysyrowicz, *Phys. Rev. B* 44, 13556 **(1991)**.
45. E. Feigenbaum and M. Orenstein, *Journal of Lightwave Technology* 25, 2547 **(2007b)**.
46. A. R. Zakharian, J. V. Moloney, and M. Mansuripur, *Opt. Express* 15, 183 **(2007)**.
47. V. V. Shevchenko, Continuous Transitions in Open Waveguides, Golem Press, Boulder, Colorado **(1971)**.
48. T. Rozzi and M. Mongiardo, Open Electromagnetic Waveguides, The Institution of Electrical Engineers, London **(1997)**.
49. D. A. B. Miller, Quantum Mechanics for Scientists and Engineers, Cambridge University Press, Cambridge **(2008)**.
50. M. Mrozowski, Guided Electromagnetic Waves, Research Studies Press, UK **(1997)**.
51. W. C. Chew, Waves and Fields in Inhomogenous Media, Van Nostrand Reinhold, New York **(1990)**.
52. R. E. Collin, Field Theory of Guided Waves, 2nd edn., Wiley-Interscience, New York **(1991a)**.
53. E. Anemogiannis and E. N. Glytsis, *Journal of Lightwave Technology* 10, 1344 **(1992)**.
54. A. Bakhtazad, H. Abiri, and R. Ghayour, *Journal of Lightwave Technology* 15, 383 **(1997)**.
55. M. S. Kwon and S. Y. Shin, *Opt. Commun.* 233, 119 **(2004)**.
56. R. Rodriguez-Berral, F. Mesa, and F. Medina, *IEEE Transactions on Microwave Theory and Techniques* 53, 1613 **(2005)**.
57. R. Rodriguez-Berral, F. Mesa, and F. Medina, *International Journal of RF and Microwave Computer-Aided Engineering* 14, 73 **(2004)**.
58. R. E. Smith, S. N. Houde-Walter, and G. W. Forbes, *IEEE Journal of Quantum Electronics* 28, 1520 **(1992)**.
59. H. J. Hagemann, W. Gudat, and C. Kunz, *Journal of the Optical Society of America* 65, 742 **(1975)**.
60. A. Zettl, Sturm-Liouville Theory, American Mathematical Society **(2005)**.
61. L. P. Felsen and N. Marcuvitz, Radiation and Scattering of Waves, IEEE Press, New York **(1994)**.
62. G. V. Eleftheriades, A. S. Omar, L. P. B. Katehi, and G. M. Rebeiz, *IEEE Transactions on Microwave Theory and Techniques* 42, 1896 **(1994)**.
63. A. A. Oliner, *IEEE Transactions on Microwave Theory and Techniques* MTT/32, 1022 **(1984)**.
64. S. A. Schelkunoff, *IEEE Transactions on Antennas and Propagation* AP/18, 309 **(1970)**.
65. P. J. Schuck, D. P. Fromm, A. Sundaramurthy, G. S. Kino, and W. E. Moerner, *Phys. Rev. Lett.* 94, 017402 **(2005)**.
66. T. Takano and J. Hamasaki, *IEEE Journal of Quantum Electronics* QE/8, 206 **(1972)**.
67. S. Ramo, J. R. Whinnery, and T. V. Duzer, Fields and Waves in Communication Electronics, Wiley, New York **(1994)**.
68. Ş. E. Kocabaş, G. Veronis, D. A. B. Miller, and S. Fan, *IEEE Journal of Selected Topics in Quantum Electronics* 14, 1462 **(2008b)**.
69. D. M. Pozar, Microwave Engineering, Wiley, New York **(1998)**.
70. P. H. Smith, Electronic Applications of the Smith Chart in Waveguide, Circuit and Component Analysis, Robert E. Krieger Publishing Company, Malabar, FL **(1983)**.
71. E. L. Ginzton, Microwave Measurements, McGraw-Hill Book Company Inc. **(1957)**; Representation and Measurement of Microwave Circuits, pp. 313–345.

72. N. Marcuvitz, Waveguide Handbook, Peter Peregrinus Ltd., London, UK **(1986)**, Chap. 5, pp. 307–309.
73. J. Schwinger and D. S. Saxon, Discontinuities in Waveguides, Gordon and Breach Science Publishers Inc., New York **(1968)**, Chap. 5, pp. 99–124.
74. L. Lewin, Advanced Theory of Waveguides, Iliffe & Sons Ltd. **(1951)**, Chap. 5, pp. 98–106.
75. R. E. Collin, Field Theory of Guided Waves, 2nd edn., Wiley-Interscience **(1991b)**, Chap. 8, pp. 581–588.
76. R. E. Collin, Foundations for Microwave Engineering, McGraw-Hill Book Company **(1966)**.
77. S. Collin, F. Pardo, and J. L. Pelouard, *Opt. Express* 15, 4310 **(2007)**.
78. F. M. Kong, K. Li, B. I. Wu, H. Huang, H. S. Chen, and J. A. Kong, *Progress in Electromagnetics Research* 76, 449 **(2007a)**.
79. F. M. Kong, B. I. Wu, H. S. Chen, and J. A. Kong, *Opt. Express* 15, 12331 **(2007b)**.
80. F. Lopez-Tejeira, S. G. Rodrigo, L. Martin-Moreno, F. J. Garcia-Vidal, E. Devaux, T. W. Ebbesen, J. R. Krenn, I. P. Radko, S. I. Bozhevolnyi, M. U. Gonzalez, et al., *Nat. Phys.* 3, 324 **(2007)**.
81. M. W. Vogel and D. K. Gramotnev, *Phys. Lett. A* 363, 507 **(2007)**.
82. A. Alu and N. Engheta, *Journal of the Optical Society of America B* 23, 571 **(2006)**.
83. N. Engheta, *Science* 317, 1698 **(2007)**.
84. A. Hosseini, H. Nejati, and Y. Massoud, *Opt. Express* 15, 15280 **(2007)**.
85. A. Hosseini, H. Nejati, and Y. Massoud, *Opt. Express* 16, 1475 **(2008)**.
86. SPICE http://en.wikipedia.org/wiki/SPICE.
87. HSPICE® Signal Integrity User Guide Synopsys, z-2007.03 edn., **(2007)**, ch. S-parameter Modeling Using the S-element.
88. G. Veronis and S. Fan, *Journal of Lightwave Technology* 25, 2511 **(2007b)**.

Received: 8 October 2008. Accepted: 22 October 2008.